Family of Enhanced Photoacoustic Imaging Agents for High-Sensitivity and Multiplexing Studies in Living Mice

Adam de la Zerda,[†,‡] Sunil Bodapati,[†] Robert Teed,[†] Salomón Y. May,[†] Scott M. Tabakman,[§] Zhuang Liu,[§,⊥] Butrus T. Khuri-Yakub,[‡] Xiaoyuan Chen,[†,∥] Hongjie Dai,[§] and Sanjiv S. Gambhir[†,#,*]

[†]Molecular Imaging Program at Stanford, Department of Radiology and Bio-X Program, [‡]Department of Electrical Engineering, and [§]Department of Chemistry, Stanford University, Palo Alto, California 94305, United States, [⊥]Institute of Functional Nano & Soft Materials (FUNSOM), Soochow University, Suzhou, Jiangsu, 215123, China, [∥]Laboratory of Molecular Imaging and Nanomedicine, National Institute of Biomedical Imaging and Bioengineering (NIBIB), National Institutes of Health (NIH), Bethesda, Maryland 20892, United States, and [#]Department of Bioengineering and Department of Materials Science & Engineering, Stanford University, Palo Alto, California 94305, United States

ABSTRACT Photoacoustic imaging is a unique modality that overcomes to a great extent the resolution and depth limitations of optical imaging while maintaining relatively high contrast. However, since many diseases will not manifest an endogenous photoacoustic contrast, it is essential to develop exogenous photoacoustic contrast agents that can target diseased tissue(s). Here we present a family of novel photoacoustic contrast agents that are based on the binding of small optical dyes to single-walled carbon nanotubes (SWNT-dye). We synthesized five different SWNT-dye contrast agents using different optical dyes, creating five "flavors" of SWNT-dye nanoparticles. In particular, SWNTs that were coated with either QSY_{21} (SWNT-QSY) or indocyanine green (SWNT-ICG) exhibited over 100-times higher photoacoustic contrast in living animals compared to plain SWNTs, leading to subnanomolar sensitivities. We then conjugated the SWNT-dye conjugates with cyclic Arg-Gly-Asp peptides to molecularly target the $\alpha_v\beta_3$ integrin, which is associated with tumor angiogenesis. Intravenous administration of these tumor-targeted imaging agents to tumor-bearing mice showed significantly higher photoacoustic signal in the tumor than in mice injected with the untargeted contrast agent. Finally, we were able to spectrally separate the photoacoustic signals of SWNT-QSY and SWNT-ICG in living animals injected subcutaneously with both particles in the same location, opening the possibility for multiplexing *in vivo* studies.

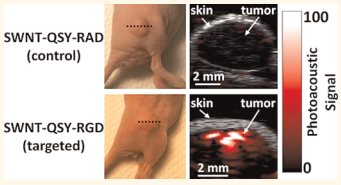

KEYWORDS: carbon nanotubes · SWNT · molecular imaging · photoacoustic imaging · multiplexing

Visualizing abnormalities in a living subject has traditionally been done through various medical imaging modalities such as X-ray computed tomography (CT), magnetic resonance imaging (MRI), and ultrasound. In the past decades many new medical imaging modalities that are based on visible and near-infrared wavelengths have emerged such as optical coherence tomography, whole-body fluorescence imaging, and others. However, due to the relatively high optical scattering of living tissue, most of the optical imaging modalities are limited in their ability to visualize objects deeper than a few millimeters in the body with reasonable resolution and signal-to-noise ratio.

Photoacoustic imaging is an emerging modality that brings significant promise to enhance the depth of penetration as well as spatial resolution, while maintaining the high contrast of optical imaging.[1] Contrary to traditional optical imaging, where light must travel in and out of the tissue, with photoacoustic imaging, light travels only into the tissue, where it is converted by optical absorbers to pressure waves through the photoacoustic effect.[2]

The primary use of photoacoustic imaging has traditionally been visualizing endogenous absorbers in the body such as hemoglobin. This allowed the visualization of the blood vessel network in three dimensions in various living tissues.[3−5] Moreover, by acquiring a partial photoacoustic spectrum, the blood oxygen saturation levels can be measured, allowing the visualization of hypoxemia.[6] In addition, the endogenous absorbing molecule melanin has been imaged using photoacoustic imaging in various scenarios, including melanoma, a skin cancer with typically elevated melanin levels.[7]

In order to allow the visualization of other biomarkers besides hemoglobin and melanin by photoacoustic imaging, exogenous

* Address correspondence to sgambhir@stanford.edu.

Received for review November 9, 2011 and accepted May 20, 2012.

Published online May 21, 2012
10.1021/nn204352r

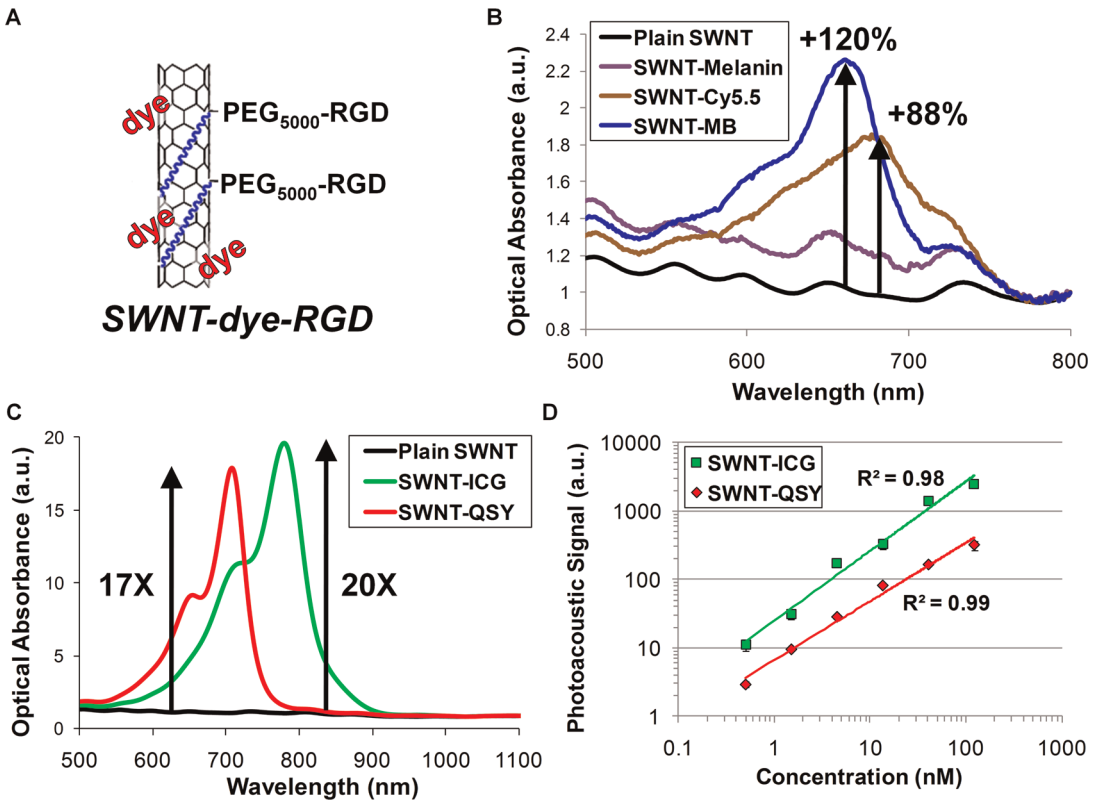

Figure 1. Characterization of the dye-enhanced SWNT. (A) Illustration of a SWNT-dye-RGD particle. The dye (red) is attached to the SWNT surface through noncovalent $\pi-\pi$ stacking bonds. Phospholipid-polyethylene glycol-5000 (blue) is conjugated to the targeting peptide (RGD) on one end and to the SWNT surface on the other end. (B, C) Optical spectra of (B) plain SWNT (black), SWNT-melanin (purple), SWNT-Cy5.5 (brown), SWNT-MB (blue), (C) SWNT-QSY (red), and SWNT-ICG (green). The QSY and ICG dye-enhanced SWNT particles showed 17- and 20-times higher optical absorption than plain SWNT at their peak absorption wavelengths, 710 and 780 nm, respectively. (D) The photoacoustic signal produced by SWNT-QSY and SWNT-ICG was observed to be linearly dependent on the particles' concentration (R^2 = 0.99 and 0.98, respectively).

contrast agents must be used.[8] These contrast agents should exhibit high optical absorption characteristics in order to produce a high photoacoustic signal and may or may not be molecularly targeted to a specific biomarker in the tissue. Significant work on photoacoustic contrast agents has been focused on gold nanoparticles[9−14] as well as other kinds of nanoparticles[15−17] and small molecules.[18] However, most of these contrast agents suffer from poor delivery, leading to only small amounts of the injected dose to accumulate in the target tissue. This problem is further amplified in molecularly targeted contrast agents. We recently reported on single-walled carbon nanotubes (SWNTs) that are coated by indocyanine green (ICG).[19] The resulting nanoparticle exhibited high optical absorbance while maintaining the high tumor-targeting abilities previously reported of plain SWNTs.[8]

In this work, we report on a general method to prepare dye-enhanced SWNT photoacoustic imaging agents by coating any one of five different small-molecule dyes onto the surface of a SWNT. We show that the resulting imaging agents can target cancer-specific receptors in tumor-bearing mice, exhibit unprecedented high sensitivity, and can be imaged simultaneously (multiplexed). The ability to multiplex several imaging agents based on their different photoacoustic spectra[20,21] is highly desirable, as it may allow in the future visualizing multiple molecular processes in a living tissue simultaneously.

RESULTS

We have recently reported on the conjugation of cyclic Arg-Gly-Asp (RGD) peptides to PEGylated SWNTs[22] (SWNT-RGD). We then reported on their use as photoacoustic imaging agents to visualize $\alpha_v\beta_3$ integrin,[8] which is overexpressed in tumor neovasculature. We then also reported on the binding of indocyanine green to the surface of the SWNTs through $\pi-\pi$ stacking.[19] This loading of ICG onto the surface of the SWNTs has resulted in significantly better *in vivo* sensitivity than plain SWNTs. In this work we generalize the method and show it works for a number of optical dyes and quenchers including QSY_{21}, methylene blue (MB), cyanine dyes such as Cy5.5, and melanin (Figure 1a). Control untargeted SWNT-dye particles were conjugated to a mutated nontargeted peptide, RAD, that does not bind to $\alpha_v\beta_3$ integrin (see Methods for more details on the syntheses).

The ultrahigh surface area to volume ratio of the SWNTs allowed for efficient loading of the optical dyes

onto the nanotubes' surface. The SWNT-dye conjugates exhibited a significant increase in the optical absorption compared to plain SWNTs of 120%, 88%, and 30% for methylene blue, Cy5.5, and melanin, respectively (Figure 1b). Of highest interest were ICG and QSY_{21} dyes, whose conjugates with SWNTs led to 20- and 17-fold increases in the particles' optical absorption, respectively (Figure 1c). Furthermore, the spectra of SWNT-QSY and SWNT-ICG peak at different wavelengths, 710 and 780 nm, respectively. We therefore selected SWNT-QSY and SWNT-ICG as the candidate molecular imaging agents to demonstrate multiplexing in this work. Importantly, the nanoparticles conjugated with RAD and RGD had nearly identical absorption spectra (see Supporting Information and Supplementary Figure S1), suggesting that the peptide conjugation did not interfere with the particle's photoacoustic signal.

We constructed a nonabsorbing and nonscattering agarose phantom with inclusions of SWNT-QSY-RGD and SWNT-ICG-RGD at increasing concentrations from 0.5 to 121.5 nM in multiples of 3 ($n = 3$ inclusions per concentration). We used our custom-made photoacoustic imaging system (see Methods and Supplementary Figure S5) and scanned the phantom at 710 and 780 nm for the QSY- and ICG-coated particles, respectively. The photoacoustic signal produced by the SWNT-QSY-RGD and SWNT-ICG-RGD particles highly correlated with the nanoparticle concentration ($R^2 = 0.99$ and 0.98, respectively) (Figure 1d).

We further validated that the new particles are stable in serum (see Supporting Information and Supplementary Figure S2). The particle's photobleaching (*i.e.*, loss of optical absorption due to continuous light exposure to the particle) was characterized and found to be relatively small. The optical absorption of SWNT-ICG was reduced by only 30% after 60 min of laser irradiation at normal power density of 8 mJ/cm^2. SWNT-QSY, however, showed higher light sensitivity, resulting in a 50% reduction in optical absorption after 7 min of laser irradiation of the same intensity (see Supporting Information and Supplementary Figure S3). Finally, cell uptake studies showed specific binding of SWNT-QSY-RGD and SWNT-ICG-RGD to U87MG cells, compared with control particles SWNT-QSY-RAD and SWNT-ICG-RAD, respectively (see Supporting Information and Supplementary Figure S4).

We then tested the particle's sensitivity in living subjects by subcutaneously injecting the lower back of mice ($n = 3$) with 30 μL of SWNT-QSY-RGD mixed with matrigel at increasing concentrations between 500 pM and 122 nM. Matrigel alone produced no significant photoacoustic signal (data not shown). All animal experiments were performed in compliance with the Guidelines for the Care and Use of Research Animals established by the Stanford University Animal Studies Committee. Upon injection, the matrigel solidified, fixing the nanoparticles in place, and three-dimensional (3D) ultrasound and photoacoustic images of the inclusions were acquired (Figure 2a). While the ultrasound image visualized the mouse anatomy (*e.g.*, skin and inclusion edges), the photoacoustic image revealed the nanoparticles' contrast in the mouse tissue. The photoacoustic signal from each inclusion was quantified using a three-dimensional region of interest (ROI) drawn over the inclusion volume. We observed a linear correlation ($R^2 = 0.97$) between the nanoparticles' concentration and the corresponding photoacoustic signal (Figure 2b), as was previously observed with SWNT-ICG-RGD.[19] Tissue background signal was calculated as the average photoacoustic signal in areas where no nanoparticles were injected. Extrapolation of the signal−concentration graph reveals that 450 pM of SWNT-QSY-RGD produces the equivalent photoacoustic signal to the tissue background (*i.e.*, signal to background ratio = 1). This value represents over 100-times improvement in sensitivity compared to plain SWNTs and is comparable to the 170 pM sensitivity limit that has been previously calculated for SWNT-ICG-RGD.

We then tested the nanoparticles' targeting ability in living mice. Mice bearing U87MG tumor xenografts (150 mm^3 in size) were injected through the tail vein (iv) with 200 μL of either SWNT-QSY-RGD (targeted) or SWNT-QSY-RAD (untargeted control) or the RGD/RAD SWNT-ICG conjugates ($n = 3$ mice per group) at a concentration of 1.2 μM. Importantly, no acute cytotoxicity or distress was observed in the animals upon injection and up to a period of one week post-injection. We acquired 3D photoacoustic and ultrasound images of the entire tumor area before and 2 h after the injection. Mice injected with the RGD-targeted nanoparticles showed significantly higher photoacoustic signal in the tumor compared with the control group injected with the RAD control particles (Figure 3a). The ultrasound images were used for visualizing the boundaries of the tumor as well as to validate that no significant movement (beyond 100 μm) had occurred throughout the experiment. Before the injection, the photoacoustic signal in the tumor is due to the tumor's blood vessels, while after the injection, the photoacoustic signal is due to both the blood vessels and the nanoparticles. To remove the background blood signal, subtraction images were calculated as the post-injection minus the pre-injection images, leaving the image primarily with the contrast made by the nanoparticles (Figure 3a). Measurement of the photoacoustic signal from a 3D ROI around the tumor (Figure 3b) showed that the photoacoustic signal in the tumor was significantly higher in mice injected with the RGD-targeted nanoparticles as compared with the control particles ($p < 0.01$). At 2 h post-injection, mice injected with SWNT-QSY-RGD showed over 3-times higher photoacoustic signal increase in the tumor than mice injected with the control SWNT-QSY-RAD.

While the optical absorption spectra of SWNT-QSY and SWNT-ICG overlap, they are not identical, which

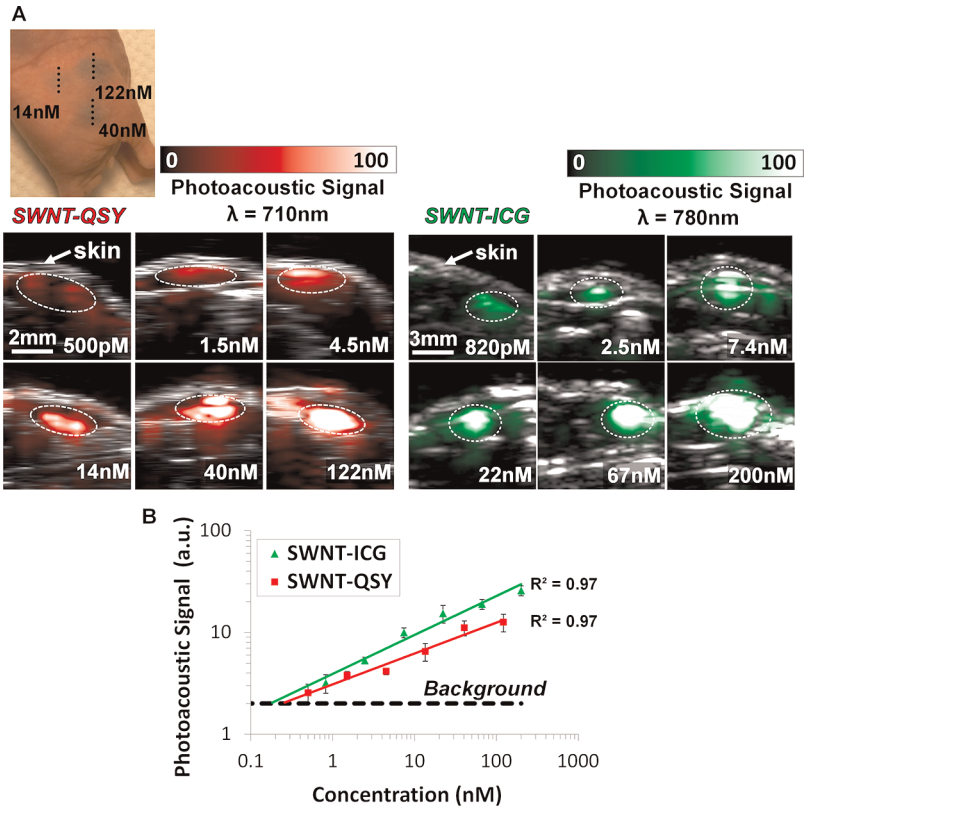

Figure 2. Photoacoustic detection of SWNT-dye particles in living mice. (A) Mice were injected subcutaneously with SWNT-QSY at concentrations between 0.5 and 122 nM. The images represent ultrasound (gray) and photoacoustic images acquired at λ = 710 nm (red) as vertical slices through the subcutaneous injections (dotted black line on the mouse picture). Photoacoustic images of mice injected with SWNT-ICG and acquired at λ = 780 nm (green) are presented for comparison and taken with permission from ref 19. The skin and inclusion region are visualized in the ultrasound images, while the photoacoustic images visualize the nanoparticles' contrast. The white dotted lines on the images illustrate the approximate edges of each inclusion. (B) The photoacoustic signal from each inclusion was calculated using 3D regions of interest, and the "background" represents the endogenous signal measured from tissues. The error bars represent standard error (n = 3 mice). Linear regression (R^2 = 0.97 for both particles) of the photoacoustic signal curves estimated that a concentration of 450 pM of SWNT-QSY or 170 pM of SWNT-ICG produces the equivalent background signal of tissues.

may allow to spectrally unmix their signals, even in situations where they are spatially co-localized. We prepared an optically clear agarose-based phantom with five wells in which SWNT-QSY and SWNT-ICG were mixed in respective concentrations of 0:100, 25:75, 50:50, 75:25, and 100:0 (in units of nM). Photoacoustic images of the phantom at 700, 730, 760, 780, and 800 nm were taken (Figure 4a) and used in a least-squares method (see Methods for more details) to unmix the photoacoustic signals produced by the SWNT-QSY and the SWNT-ICG particles. No cross-signaling between the SWNT-QSY and SWNT-ICG channels was observed in the wells with either pure SWNT-QSY or pure SWNT-ICG. In wells with both SWNT-QSY and SWNT-ICG, an appropriate proportion of signal of both particles was observed (Figure 4b).

Finally, we injected 30 μL of an equal mixture of SWNT-QSY and SWNT-ICG at 50 nM subcutaneously to a living mouse flank (Figure 5a). Control injections of 30 μL of SWNT-QSY and SWNT-ICG alone were injected subcutaneously to the mouse flank as well. Photoacoustic images at 700, 730, 760, 780, and 800 nm were used to spectrally unmix the SWNT-QSY and the SWNT-ICG signals. The SWNT-QSY injection site showed only SWNT-QSY signal (Figure 5b), and the SWNT-ICG injection site showed primarily SWNT-ICG signal (Figure 5c). Importantly, the site that was injected with the equal mixture of particles showed both SWNT-QSY and SWNT-ICG signal (Figure 5d). At the area of injection, a slight separation of photoacoustic signals of the two channels (SWNT-QSY and SWNT-ICG) was observed. These image reconstruction artifacts are likely caused by slight movements of the mouse between the acquisition of consecutive photoacoustic images at different wavelengths, as well as differences in light tissue distribution across the five wavelengths.

DISCUSSION

We have synthesized, characterized, and demonstrated the application of multiple dye-enhanced SWNTs as ultrahigh-sensitivity photoacoustic imaging agents. For SWNT-QSY and SWNT-ICG, concentrations as low as 450 and 170 pM were estimated to be the *in vivo* sensitivity limits, respectively, representing over 100-times

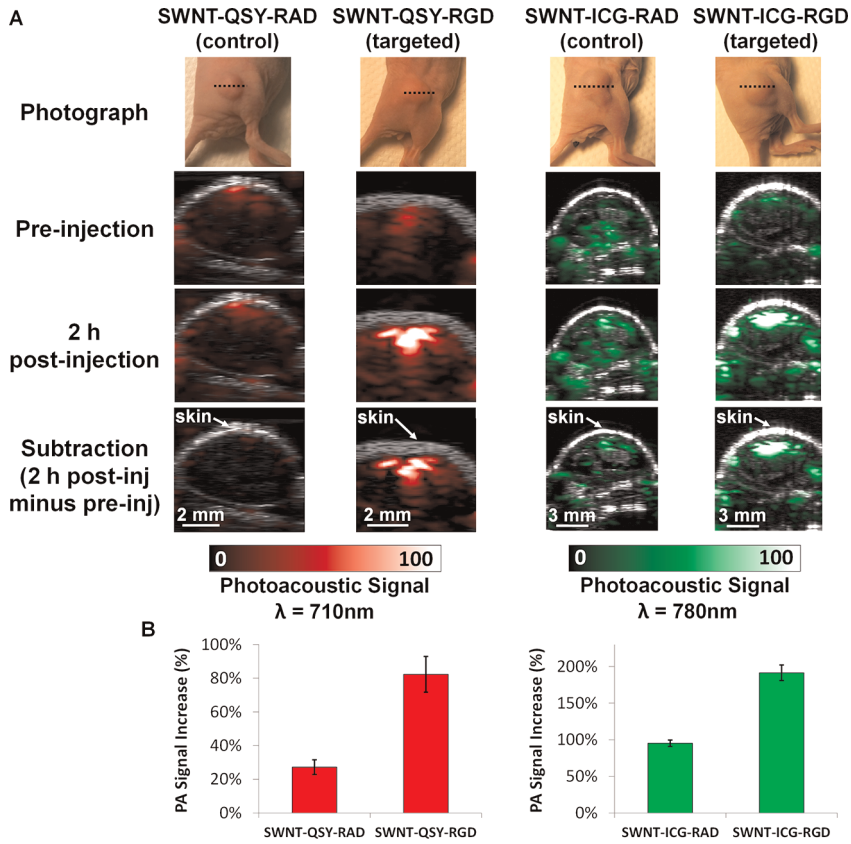

Figure 3. SWNT-dye tumor targeting in living mice. (A) Ultrasound (gray) and photoacoustic (red for $\lambda = 710$ nm and green for $\lambda = 780$ nm) images of a vertical slice through the tumors (dotted black line). The ultrasound images show the skin and the tumor boundaries. Subtraction photoacoustic images were calculated as 2 h post-injection minus pre-injection images. As can be seen in the subtraction images, SWNT-QSY-RGD as well as SWNT-ICG-RGD accumulated in significantly higher amounts in the tumor as compared to their respective control versions. SWNT-ICG images (green) are presented for comparison and are taken with permission from ref 19. (B) Quantitative region of interest analysis showed that SWNT-QSY-RGD creates a 3-fold higher photoacoustic signal increase in the tumor than the control SWNT-QSY-RAD particle ($p < 0.01$). SWNT-ICG-RGD provides over 100% higher photoacoustic signal increase than the control SWNT-ICG-RAD ($p < 0.01$). The error bars represent standard error ($n = 3$ mice).

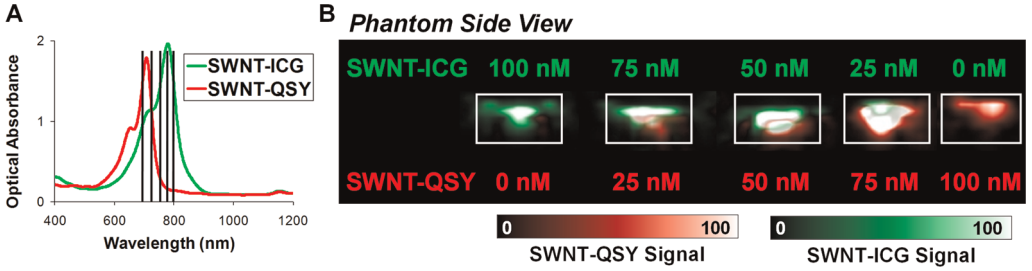

Figure 4. Multiplexing of SWNT-QSY and SWNT-ICG *in vitro*. (A) An agaorose phantom containing SWNT-ICG and SWNT-QSY at different mixture concentrations (pure SWNT-ICG, 1:3, 1:1, 3:1, and pure SWNT-QSY) was scanned using the photoacoustic instrument at 5 different wavelengths (700, 730, 760, 780, 800 nm). (B) Despite their overlapping spectra, the photoacoustic signals from SWNT-QSY (red) and SWNT-ICG (green) were unmixed well by the least-squares algorithm.

improvement over plain SWNTs.[8] This improvement is likely due to both the higher optical absorption of the particles and the fact that the new particle's absorption peak is further red-shifted than plain SWNTs, where the background tissue photoacoustic signal is greatly reduced. Most importantly, intravenous injection of RGD-targeted SWNT-QSY and SWNT-ICG particles to tumor-bearing mice led to significantly greater accumulation of the particles in the tumors compared to nontargeted control particles. The fact that plain SWNT-RGD targets tumors in living mice does not necessarily imply that SWNT-dye-RGD would also target tumors in living mice. This is because the additional dye-coating may increase the size and molecular weight of the particles and change their surface charge and zeta-potential. Finally, we demonstrated the ability to multiplex the signals from SWNT-QSY and SWNT-ICG both *in vitro* and in living mice. This entails not only greater sensitivity

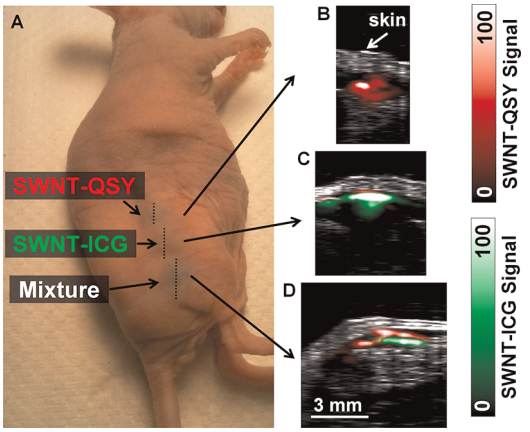

Figure 5. Multiplexing of SWNT-QSY and SWNT-ICG in living mice. (A) A mouse was injected with 30 μL of 50 nM SWNT-QSY (upper inclusion), 30 μL of 50 nM SWNT-ICG (middle inclusion), and 30 μL of an equal mixture of 50 nM of SWNT-QSY and SWNT-ICG (lower inclusion). (B) Unmixed photoacoustic vertical slice through the upper inclusion, showing only SWNT-QSY signal (red). (C) Unmixed photoacoustic slice through the middle inclusion, showing mostly SWNT-ICG signal (green). (D) Unmixed photoacoustic slice through the lower inclusion, showing both SWNT-QSY and SWNT-ICG signals spread throughout the inclusion area. Image reconstruction artifacts as well as inhomogeneous light penetration into the tissue are likely the cause for the separation of the green and red signals in the image.

for earlier detection of diseases but also greater specificity by providing molecular information on two molecular processes simultaneously.

While small-molecule optical dyes have lower optical absorption, they are also significantly smaller than nanoparticles. For example, the ratio between the absorption coefficient of ICG and its molecular weight is still 7-times greater than that of a plain SWNT. This suggests that creating a carrier for small optical dyes, such as SWNT, may be highly beneficial, as indeed shown in this work. Determining the exact number of dye molecules per SWNT is challenging due to synergistic or quenching effects the dyes may be exhibiting on themselves or the SWNT. However, assuming such effects are not taking place in this SWNT-dye system, the enhancement in optical absorption of the SWNT-dye conjugates would represent the number of dye molecules times the dye absorption coefficient. Hence, the number of dyes per SWNT can be estimated to be 33, 130, 710, and 2032 for Cy5.5, methylene blue, ICG, and QSY_{21}, respectively. It is likely that the difference among the dyes is a result of their ability to form $\pi-\pi$ stacking interactions with the SWNT surface.

Photoacoustic imaging has been primarily used to visualize endogenous absorbers such as hemoglobin and melanin.[3−5,7] However, in order to visualize molecular characteristics of a tumor, an exogenous contrast agent that is specific for a given molecular target is required.[23] However, the main challenge in designing a photoacoustic imaging agent is that sufficient amounts of the agent need to reach the target site and create a detectable and specific signal. Most nanoparticles reported to date to produce strong photoacoustic signal suffer from significant and rapid uptake by the reticuloendothelial system, likely preventing the particles from accumulating at the tumor site in sufficient amounts. The SWNTs used here are 1−2 nm in diameter and 50−300 nm in length. We believe that this size is maintained even after the conjugation of the small optical dyes to the SWNT surface, as the dyes are conjugated directly to the surface of the nanotube, under the poly(ethylene glycol) (PEG). This likely allows the particles to maintain the favorable biodistribution of plain SWNT-RGD.[22] Hence, the dye-enhanced SWNTs presented in this work offer both unprecedented photoacoustic sensitivity and good tumor-targeting capabilities upon intravenous injection. We have also previously published pilot toxicology studies of the SWNTs with encouraging results in mouse models[24] and observed the SWNTs are able to be excreted *via* the biliary pathway.[25,26]

CONCLUSION

The dye-enhanced SWNT photoacoustic imaging agents reported here have the capability to bind to molecular targets in living animals while maintaining a very high photoacoustic signal and allowing multiplexing studies. No other imaging modality or imaging agent can achieve both sub-nanomolar sensitivity at high depths of penetration and submillimeter spatial resolution, as can be achieved with photoacoustic imaging of dye-enhanced SWNTs. To our knowledge, this is the first demonstration of multiplexing photoacoustic imaging agents that are capable of molecularly targeting tumors in living animals.

METHODS

Dye-Enhanced SWNT Synthesis. A complete description of the synthesis of SWNT-RGD and SWNT-RAD can be found elsewhere.[22] PEGylayed SWNTs at a concentration of 250 nM were incubated overnight in water with 1 mM indocyanine green, QSY_{21} or Cy5.5, or excess melanin or methylene blue. ICG (Spectrum Laboratory Products, CA, USA) (20 mM) was dissolved in DMSO first and then added to SWNT water solutions with a final DMSO concentration of <10% by volume. Prior to incubation with SWNTs, Cy5.5 and QSY_{21}, purchased as *N*-hydroxysuccinimidyl esters, were dissolved in DMSO and hydrolyzed overnight by dilution into deionized water. Unbound dye molecules were removed from the solution by filtration through 100 kDa centrifuge filters (Millipore) and washed 6−8 times. The SWNTs used in this work were 50−300 nm in length and 1−2 nm in diameter. The molar concentrations are based on an average molecular weight of 170 kDa per SWNT (150 nm in length and 1.2 nm in diameter).

For preparation of SWNT-R(G/A)D-ICG and SWNT-R(G/A)D-QSY, SWNTs were dispersed by sonication as described

previously[22] in 1,2-distearoyl-*sn*-glycero-3-phosphoethanolamine-PEG_{5000}-NH_2 (DSPE-PEG-NH_2, NOF Corp.). Following removal of free surfactant by repeated ultracentrifuge filtration, the SWNT suspension at ~250 nM was incubated with 1 mM ICG or 1 mM QSY_{21}, dissolved and hydrolyzed, followed by ultracentrifuge filtration to remove any free dye molecules. Next, the dye-loaded SWNTs suspended in DSPE-PEG-NH_2 at ~500 nM were mixed with 0.5 mM sulfo-SMCC (Pierce) in phosphate-buffered saline (PBS) and allowed to react for 2 h at room temperature. Free sulfo-SMCC was removed by repeated ultracentrifuge filtration, and the resulting maleimide-activated SWNT-dye conjugate suspensions were each split into two equal aliquots. Cyclic(RGDfC) (RGD) or cyclic(RADfC) (RAD) were mixed with 20 mM tris(2-carboxyethyl)phosphine-HCl (TCEP) in PBS adjusted to pH 8 for 15 min at room temperature. The RGD or RAD containing TCEP was added into each aliquot of maleimide-activated SWNT-dye conjugates at a final peptide concentration of 150 μM, and coupling was allowed to proceed for 24 h at 4 °C, followed by a final round of repeated ultracentrifugal filtration to remove free peptide.

Photoacoustic Instrumentation. Our custom-made photoacoustic system[27] is illustrated in Supplementary Figure 5. A tunable pulsed laser with a repetition rate of 10 Hz and a pulse width of 5 ns (Nd:YAG Surelight-III-10 connected to Surelite OPO Plus, Continuum) illuminated the object through a fiber optic ring light (50-1353 Ringlight, Fiberoptic Systems Inc.). The average energy density of the laser at the wavelengths used in this study (*i.e.*, 700, 710, 730, 760, 780, and 800 nm) was set to be ~8 mJ/cm^2 at the target site, which is below the ANSI limitation for laser skin exposure.[28] A 5 MHz focused transducer (25.5 mm focal length, 4 MHz bandwidth, F number of 2.0, depth of focus of 6.5 mm, lateral resolution of 600 μm, and axial resolution of 380 μm; A309S-SU-F-24.5-MM-PTF, Panametrics) was used to acquire both pulse-echo and photoacoustic images. In addition, high-resolution ultrasound images were acquired using a 25 MHz focused transducer (27 mm focal length, 12 MHz bandwidth, F number of 4.2, depth of focus of 7.5 mm, lateral resolution of 250 μm, and axial resolution of 124 μm; V324-SU-25.5-MM, Panametrics). A precision *xyz*-stage (U500, Aerotech Inc.) with a minimum step size of 1 μm was used to move the transducer and the fiber ring along a planar 2D trajectory. At every position, the acquired signal was averaged over four laser pulses. The time of arrival and the intensity of the laser pulses were recorded using a silicon photodiode (DET10A, Thorlabs). This information was used to synchronize the acquisition and compensate for pulse-to-pulse variations in laser intensity. The analog photoacoustic signals were amplified using a variable-gain preamplifier (5072PR/115VAC, Panametrics) and digitized using an oscilloscope (Infiniium 54825A, Agilent). The photoacoustic and ultrasound images were reconstructed as follows: the A-scan from each position of the transducer was band-pass filtered with 200% fractional bandwidth, compensated for laser intensity variation, and envelope detected. The A-scans were then combined to reconstruct a 3D intensity image of the target. No further postprocessing was done on the images. The ultrasound images acquired using the 5 and 25 MHz transducers were aligned together using small vertical translations so that the object's skin level matched in both images. Then, photoacoustic and high-frequency ultrasound images were analyzed, coregistered, and displayed using AMIDE[29] software.

Spectral Unmixing of the Photoacoustic Signals. In both the *in vitro* and *in vivo* experiments that showed the multiplexing capability of SWNT-QSY and SWNT-ICG, the same acquisition technique and image reconstruction algorithms were used. Initially, an ultrasound image of the object was acquired to determine the areas of interest. Then, consecutive photoacoustic images of the object at wavelengths of 700, 730, 760, 780, and 800 nm were acquired. The principal components of the photoacoustic signals of SWNT-QSY and SWNT-ICG were determined on the basis of region of interest analysis over regions that were previously known to contain SWNT-QSY only or SWNT-ICG only. Then, least-squares technique was used to create two individual images on a pixel-by-pixel basis, one for each SWNT-dye particle. Visualization of the two images was done using Amide[29] software, where the red color was assigned to the SWNT-QSY signal and the green color was assigned to the SWNT-ICG signal.

Mouse Arrangement in the Photoacoustic System. All animal experiments were performed in compliance with the Guidelines for the Care and Use of Research Animals established by the Stanford University Animal Studies Committee. Female nude mice were used for all the photoacoustic studies. The mice that were scanned in the photoacoustic system were fully anesthetized using isoflurane delivered through a nose-cone (2% isoflurane in 100% oxygen, 2 L per min gas flow rate). Prior to the photoacoustic scan, the areas of interest were covered with agar gel to stabilize the area and minimize any breathing and other motion artifacts. A plastic wrap water bath was placed on top of the agar gel. An ultrasonic transducer, placed in the water bath, was therefore acoustically coupled to the mouse tissues. This setup allowed the ultrasonic transducer to move freely in 3D while not applying any physical pressure on the mouse.

Statistical Methods. For the tumor-targeting experiment, we used the two-sided Student's *t* test to test the hypothesis that the group of mice injected with the RGD-targeted particles exhibit higher photoacoustic signal than mice injected with the control RAD-targeted particles.

Conflict of Interest: The authors declare no competing financial interest.

Acknowledgment. We would like to acknowledge funding from the National Institutes of Health (NIH) grants NCI CCNE U54 CA119367 (SSG) and NCI ICMIC P50 CA114747 (SSG) and the Canary Foundation for supporting this work. A.d.l.Z. acknowledges funding from the Bio-X Graduate Student Fellowship, the Department of Defense—Breast Cancer Research Program—Predoctoral Traineeship Award (W81XWH-09-1-0025), and the Damon Runyon Cancer Research Foundation (DRG-2094-11). The authors would also like to thank Srikant Vaithilingam, Omer Oralkan, and Te-Jen Ma for helpful discussions.

Supporting Information Available: In vitro characterization of the particles including optical stability upon peptide conjugation, serum-stability, photobleaching, and cell-uptake study. This material is available free of charge *via* the Internet at http://pubs.acs.org.

REFERENCES AND NOTES

1. Wang, L. V. Multiscale Photoacoustic Microscopy and Computed Tomography. *Nat. Photonics* **2009**, *3*, 503–509.
2. Bell, A. On the Production and Reproduction of Sound by Light. *Am. J. Sci.* **1880**, *20*, 305–324.
3. Zhang, H. F.; Maslov, K.; Stoica, G.; Wang, L. V. Functional Photoacoustic Microscopy for High-Resolution and Noninvasive in Vivo Imaging. *Nat. Biotechnol.* **2006**, *24*, 848–851.
4. Laufer, J.; Zhang, E.; Raivich, G.; Beard, P. Three-Dimensional Noninvasive Imaging of the Vasculature in the Mouse Brain Using a High Resolution Photoacoustic Scanner. *Appl. Opt.* **2009**, *48*, D299–306.
5. de la Zerda, A.; Paulus, Y. M.; Teed, R.; Bodapati, S.; Dollberg, Y.; Khuri-Yakub, B. T.; Blumenkranz, M. S.; Moshfeghi, D. M.; Gambhir, S. S. Photoacoustic Ocular Imaging. *Opt. Lett.* **2010**, *35*, 270–272.
6. Wang, X.; Xie, X.; Ku, G.; Wang, L. V.; Stoica, G. Noninvasive Imaging of Hemoglobin Concentration and Oxygenation in the Rat Brain Using High-Resolution Photoacoustic Tomography. *J. Biomed. Opt.* **2006**, *11*, 024015.
7. Oh, J. T.; Li, M. L.; Zhang, H. F.; Maslov, K.; Stoica, G.; Wang, L. V. Three-Dimensional Imaging of Skin Melanoma in Vivo by Dual-Wavelength Photoacoustic Microscopy. *J. Biomed. Opt.* **2006**, *11*, 034032.
8. de la Zerda, A.; Zavaleta, C.; Keren, S.; Vaithilingam, S.; Bodapati, S.; Liu, Z.; Levi, J.; Smith, B. R.; Ma, T. J.; Oralkan, O.; *et al.* Carbon Nanotubes As Photoacoustic Molecular Imaging Agents in Living Mice. *Nat. Nanotechnol.* **2008**, *3*, 557–562.
9. Kircher, M. F.; de la Zerda, A.; Jokerst, J. V.; Zavaleta, C. L.; Kempen, P. J.; Mittra, E.; Pitter, K.; Huang, R.; Campos, C.;

Habte, F.; *et al*. A Brain Tumor Molecular Imaging Strategy Using a New Triple-Modality MRI-Photoacoustic-Raman Nanoparticle. *Nat. Med.* **2012**, *18*, 829–834.
10. Mallidi, S.; Larson, T.; Tam, J.; Joshi, P. P.; Karpiouk, A.; Sokolov, K.; Emelianov, S. Multiwavelength Photoacoustic Imaging and Plasmon Resonance Coupling of Gold Nanoparticles for Selective Detection of Cancer. *Nano Lett.* **2009**, *9*, 2825–2831.
11. Kim, J. W.; Galanzha, E. I.; Shashkov, E. V.; Moon, H. M.; Zharov, V. P. Golden Carbon Nanotubes As Multimodal Photoacoustic and Photothermal High-Contrast Molecular Agents. *Nat. Nanotechnol.* **2009**, *4*, 688–694.
12. Eghtedari, M.; Oraevsky, A.; Copland, J. A.; Kotov, N. A.; Conjusteau, A.; Motamedi, M. High Sensitivity of in Vivo Detection of Gold Nanorods Using a Laser Optoacoustic Imaging System. *Nano Lett.* **2007**, *7*, 1914–1918.
13. Yang, X.; Skrabalak, S. E.; Li, Z. Y.; Xia, Y.; Wang, L. V. Photoacoustic Tomography of a Rat Cerebral Cortex in Vivo with Au Nanocages As an Optical Contrast Agent. *Nano Lett.* **2007**, *7*, 3798–3802.
14. Agarwal, A.; Huang, S. W.; O'Donnell, M.; Day, K. C.; Day, M.; Kotov, N.; Ashkenazi, S. Targeted Gold Nanorod Contrast Agent for Prostate Cancer Detection by Photoacoustic Imaging. *J. Appl. Phys.* **2007**, *102*, 064701–064704.
15. Kim, G.; Huang, S. W.; Day, K. C.; O'Donnell, M.; Agayan, R. R.; Day, M. A.; Kopelman, R.; Ashkenazi, S. Indocyanine-Green-Embedded Pebbles As a Contrast Agent for Photoacoustic Imaging. *J. Biomed. Opt.* **2007**, *12*, 044020.
16. Zhang, Q.; Iwakuma, N.; Sharma, P.; Moudgil, B. M.; Wu, C.; McNeill, J.; Jiang, H.; Grobmyer, S. R. Gold Nanoparticles As a Contrast Agent for in Vivo Tumor Imaging with Photoacoustic Tomography. *Nanotechnology* **2009**, *20*, 395102.
17. Bouchard, L. S.; Anwar, M. S.; Liu, G. L.; Hann, B.; Xie, Z. H.; Gray, J. W.; Wang, X.; Pines, A.; Chen, F. F. Picomolar Sensitivity MRI and Photoacoustic Imaging of Cobalt Nanoparticles. *Proc. Natl. Acad. Sci. U. S. A.* **2009**, *106*, 4085–4089.
18. Levi, J.; Kothapalli, S. R.; Ma, T. J.; Hartman, K.; Khuri-Yakub, B. T.; Gambhir, S. S. Design, Synthesis, and Imaging of an Activatable Photoacoustic Probe. *J. Am. Chem. Soc.* **2010**, *132*, 11264–11269.
19. de la Zerda, A.; Liu, Z.; Bodapati, S.; Teed, R.; Vaithilingam, S.; Khuri-Yakub, B. T.; Chen, X.; Dai, H.; Gambhir, S. S. Ultrahigh Sensitivity Carbon Nanotube Agents for Photoacoustic Molecular Imaging in Living Mice. *Nano Lett.* **2010**, *10*, 2168–2172.
20. Razansky, D.; Distel, M.; Vinegoni, C.; Ma, R.; Perrimon, N.; Koster, R. W.; Ntziachristos, V. Multispectral Opto-Acoustic Tomography of Deep-Seated Fluorescent Proteins in Vivo. *Nat. Photonics* **2009**, *3*, 412–417.
21. Ntziachristos, V.; Razansky, D. Molecular Imaging by Means of Multispectral Optoacoustic Tomography (MSOT). *Chem. Rev.* **2010**, *110*, 2783–2794.
22. Liu, Z.; Cai, W.; He, L.; Nakayama, N.; Chen, K.; Sun, X.; Chen, X.; Dai, H. In Vivo Biodistribution and Highly Efficient Tumour Targeting of Carbon Nanotubes in Mice. *Nat. Nanotechnol.* **2007**, *2*, 47–52.
23. de la Zerda, A.; Kim, J.-W.; Galanzha, E. I.; Gambhir, S. S.; Zharov, V. P. Advanced Contrast Nanoagents for Photoacoustic Molecular Imaging, Cytometry, Blood Test and Photothermal Theranostics. *Contrast Media Mol. Imaging* **2011**, *6*, 346–369.
24. Schipper, M. L.; Nakayama-Ratchford, N.; Davis, C. R.; Kam, N. W. S.; Chu, P.; Liu, Z.; Sun, X.; Dai, H.; Gambhir, S. S. A Pilot Toxicology Study of Single-Walled Carbon Nanotubes in a Small Sample of Mice. *Nat. Nanotechnol.* **2008**, *3*, 216–221.
25. Liu, Z.; Davis, C.; Cai, W.; He, L.; Chen, X.; Dai, H. Circulation and Long-Term Fate of Functionalized, Biocompatible Single-Walled Carbon Nanotubes in Mice Probed by Raman Spectroscopy. *Proc. Natl. Acad. Sci. U. S. A.* **2008**, *105*, 1410–1415.
26. Liu, Z.; Tabakman, S.; Welsher, K.; Dai, H. Carbon Nanotubes in Biology and Medicine: In Vitro and in Vivo Detection, Imaging and Drug Delivery. *Nano Res.* **2009**, *2*, 85–120.
27. Vaithilingam, S.; Ma, T.-J.; Furukawa, Y.; de la Zerda, A.; Oralkan, O.; Kamaya, A.; Keren, S.; Gambhir, S. S.; Jr, R. B. J.; Khuri-Yakub, B. T. In *A Co-Axial Scanning Acoustic and Photoacoustic Microscope*; Ultrasonics Symposium, 2007. IEEE, 2007; pp 2413−2416.
28. *American National Standards Institute, American National Standard for the Safe Use of Lasers*, ANSI Standard Z136.1-2000, ANSI, Inc.: New York, **2000**.
29. Loening, A. M.; Gambhir, S. S. Amide: A Free Software Tool for Multimodality Medical Image Analysis. *Mol. Imaging* **2003**, *2*, 131–137.